

Quaternion-based machine learning on topological quantum systems

Min-Ruei Lin,^{1,*} Wan-Ju Li,¹ and Shin-Ming Huang^{1, 2, †}

¹*Department of Physics, National Sun Yat-sen University, Kaohsiung 80424, Taiwan*

²*Center of Crystal Research, National Sun Yat-sen University, Kaohsiung 80424, Taiwan*

(Dated: September 30, 2022)

Topological phase classifications have been intensively studied via machine-learning techniques where different forms of the training data are proposed in order to maximize the information extracted from the systems of interests. Due to the complexity in quantum physics, advanced mathematical architecture should be considered in designing machines. In this work, we incorporate quaternion algebras into data analysis either in the frame of supervised and unsupervised learning to classify two-dimensional Chern insulators. For the unsupervised-learning aspect, we apply the principal component analysis (PCA) on the quaternion-transformed eigenstates to distinguish topological phases. For the supervised-learning aspect, we construct our machine by adding one quaternion convolutional layer on top of a conventional convolutional neural networks. The machine takes quaternion-transformed configurations as inputs and successfully classify all distinct topological phases, even for those structures that are not seen by the machine during the training process. Our work demonstrates the power of quaternion algebras on extracting crucial features from the targeted data and the advantages of quaternion-based neural networks than conventional ones in the tasks of topological phase classifications.

I. INTRODUCTION

The phase classification using machine-learning (ML) based techniques has been attracting intense attentions since the pioneering work in 2017[1]. In addition to the classical phase detections[2, 3] where each phase is well defined by the corresponding order parameters, detecting topological phase transitions[2] is interesting and challenging[4] due to the lack of local order parameters. Recently, the phase detections and classifications have been performed via different ML techniques for classifying various topological invariants[4–36], including the Chern number[6, 10, 14–23], winding number[16, 18, 21, 24–26], \mathbb{Z}_2 index[4, 6, 10, 17, 26–36], to name a few. In addition to the applied ML architectures, the forms of the inputs for training the machine also play a crucial role in determining the resulting performance of the topological phase detections[4].

For the topological systems with the Chern numbers or the winding numbers as the topological invariants, various types of inputs are used to perform the phase classifications. For instance, researchers in Kim’s group introduced quantum loop topography (QLT) to construct multi-dimensional images from raw Hamiltonians or wave functions as inputs[14, 17]. Zhai’s group collected the Bloch Hamiltonians into an arrays to feed their machines[16, 24]. The real-space particle densities and local density of states were used as inputs by Cheng *et al.*[15]. Carvalho *et al.* fed the local projections of the density matrix to the machine [6]. From cold-atom experiments, momentum-space density images were generated as inputs by Rem *et al.*[20]. The time-of-flight

images[10, 19], spatial correlation function[10] and density–density correlation function[10] were also used as inputs. The density profiles formed in quantum walks were proposed as appropriate inputs for training in Ming *et al.*’s work[23]. Furthermore, several works had tried the spin configurations[18] and the Bloch Hamiltonians over the Brillouin zone (BZ) as inputs[18, 21]. For these forms of inputs mentioned above, various ML techniques with distinct real-valued neural networks have been applied to discriminate different topological phases.

As the development of artificial neural networks becomes mature, generalization from real-valued neural networks to complex-valued ones is undertaken that anticipates a raise of representation capability of machines [37, 38]. Specifically, a quaternion contains one real part and three imaginary parts so that a quaternion-based neural network[39–42] is expected to have remarkable performance on handling the processing of data with more than two degrees of freedom such as the color images (RGB channels) and the descriptions of 3D systems (xyz coordinates). There have been various proposals about quaternion-based neural networks in ML techniques and applications in computer science, such as the quaternion convolutional neural network (qCNN)[38, 43, 44], quaternion recurrent neural network[45], quaternion generative adversarial networks[46], quaternion-valued variational autoencoder[47], quaternion graph neural networks[48], quaternion capsule networks[49] and quaternion neural networks for the speech recognitions[50]. However, the ML-related applications of the quaternion-based neural networks on solving problems in physics are still limited, especially in the topological phase detections, even though the quaternion-related concepts have been applied in some fields in physics [51–53].

In this work, we perform the Chern-insulator classifications from both supervised- and unsupervised-learning

* m082030021@student.nsysu.edu.tw

† shinming@mail.nsysu.edu.tw

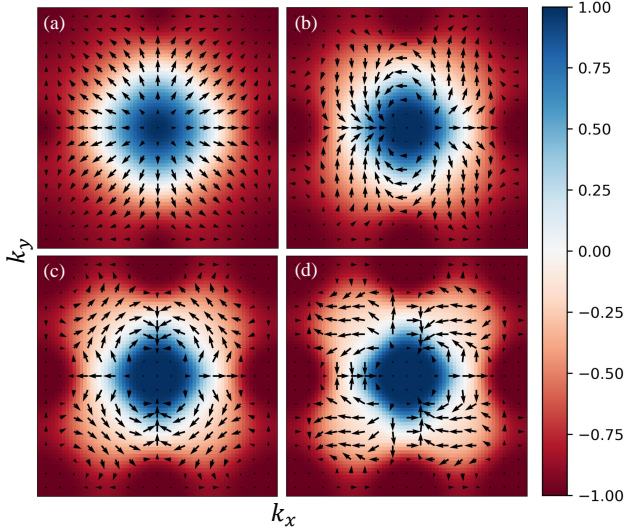


FIG. 1. Spin vectors in the Brillouin zone, $k_x, k_y \in (-\pi, \pi]$, with Chern number (a) $C = 1$, (b) $C = 2$, (c) $C = 3$ and (d) $C = 4$.

aspects based on the inputs transformed via the quaternion algebra. For the unsupervised learning, we firstly encode the quaternion-transformed eigenstates of Chern insulators via a convolution function as inputs and study them using the principal component analysis. We found that using only the first two principal elements is not enough to fully classify the Chern insulators, consistent with Ming's work[23]. Further studies show that the performance can be improved by including more principal components. For the supervised learning, we construct a quaternion-based neural network in which the first layer is a quaternion convolutional layer. We then show that this quaternion-based machine has better performance than a conventional CNN machine. Our machine is good not only at testing but also at identifying data that have no common structures as in training data. The good performance can be partially attributed to the similarities between the formula of the Berry curvatures and the quaternion algebra. Therefore, our work demonstrates the power of the quaternion algebra on extracting relevant information from data, paving the way to applications of quaternion-based algorithm ML techniques in topological phase classifications.

The outline of the remaining part of this work is as follows. In section II, we introduce the model Hamiltonian, generating the training data for our classification tasks, and the quaternion convolution layer used in this work. PCA analysis of the quaternion-transformed eigenstates is discussed in Sec. III. The data preparations, the network structures and the performance of the quaternion-based supervised learning task are given in Sec. IV. Some further discussions on our neural networks are given in Sec. V. Finally, a conclusion is provided in Sec. VI.

II. MODEL AND QUATERNION CONVOLUTIONAL LAYER

A. Model

A generic two-band Bloch Hamiltonian with the aid of the identity matrix σ_0 and Pauli matrices $\boldsymbol{\sigma} = (\sigma_1, \sigma_2, \sigma_3)$ is written as

$$\mathcal{H}(\vec{k}) = h_0(\vec{k})\sigma_0 + \mathbf{h}(\vec{k}) \cdot \boldsymbol{\sigma}, \quad (1)$$

where $\vec{k} = (k_x, k_y)$ is the crystal momentum in the 2D BZ ($= k_x, k_y \in (-\pi, \pi]$), and the vector $\mathbf{h} = (h_1, h_2, h_3)$ acts as an external magnetic field. Sometimes we will omit arguments \vec{k} when writing $\mathbf{h}(\vec{k})$ for brevity in k -space. The eigenstate of the upper (lower) band will represent the spin pointing antiparallel (parallel) to $\mathbf{n} = \mathbf{h}/|\mathbf{h}|$. Since $h_0(\vec{k})$ does not affect the pointing direction, it will be ignored in the remaining part of this section. The function \mathbf{n} embeds the topology of the system, and we firstly discuss the topological structure in \mathbf{n} . Here, the topological invariant is the Chern number $C \in \mathbb{Z}$ with the formula:

$$C = \frac{1}{4\pi} \int_{\text{BZ}} \mathbf{n} \cdot (\partial_{k_x} \mathbf{n} \times \partial_{k_y} \mathbf{n}) d\vec{k}, \quad (2)$$

where the integrand is the Berry curvature and the integration is over the first BZ.

We construct the normalized spin configurations $\mathbf{n}(\vec{k})$ based on the following models. For topological systems, we choose the Hamiltonian with $\mathbf{h} = \mathbf{h}^{(c)}$, where

$$\mathbf{h}^{(c)}(\vec{k}) = \begin{pmatrix} \text{Re}[(\sin k_x - i \sin k_y)^c] \\ -\text{Im}[(\sin k_x - i \sin k_y)^c] \\ \cos k_x + \cos k_y + m \end{pmatrix} \quad (3)$$

with positive integer c and real parameter m to control the Chern number. For $c = 1$, the model is the Qi-Wu-Zhang (QWZ) model [54]. For a given c , the Chern number C can be either 0, c , or $-c$ depending on the

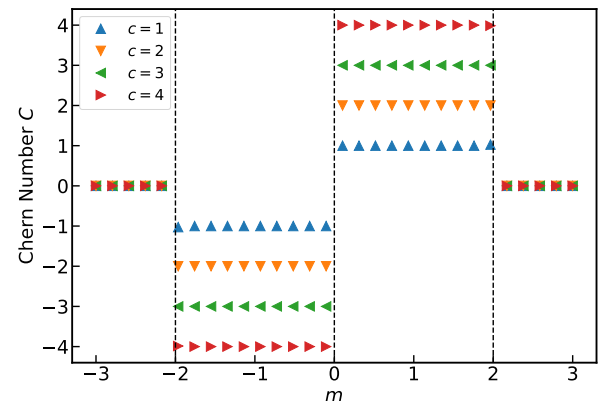


FIG. 2. The Chern number with various m and c .

value of m :

$$C = \begin{cases} \text{sgn}(m)c, & 0 < |m| < 2, \\ 0, & |m| > 2. \end{cases} \quad (4)$$

The Chern numbers with different c 's and m 's are shown in Fig. 1. Note that $C = 0$ stands for a topologically trivial phase and nonzero C 's are for nontrivial phases. The topological phase diagram is shown in Fig. 2.

In this work, the unsupervised learning involves seven topological phases ($C = 0, \pm 1, \pm 2, \pm 3$) in Sec. III, and the supervised learning involves nine topological phases ($C = 0, \pm 1, \pm 2, \pm 3, \pm 4$) in Sec. IV.

B. Quaternion convolutional layer

A quaternion number has four components, the first of which stands for the real part and the other three of which stand for the imaginary parts. Given two quaternions $q_1 = (r_1, a_1, b_1, c_1)$ and $q_2 = (r_2, a_2, b_2, c_2)$, their product $Q = q_1 q_2 = (R, A, B, C)$ is given by

$$\begin{pmatrix} R \\ A \\ B \\ C \end{pmatrix} = \begin{pmatrix} r_1 r_2 - a_1 a_2 - b_1 b_2 - c_1 c_2 \\ a_1 r_2 + r_1 a_2 - c_1 b_2 + b_1 c_2 \\ b_1 r_2 + c_1 a_2 + r_1 b_2 - a_1 c_2 \\ c_1 r_2 - b_1 a_2 + a_1 b_2 + r_1 c_2 \end{pmatrix}, \quad (5)$$

which can be written as the matrix product form

$$\begin{pmatrix} R \\ A \\ B \\ C \end{pmatrix} = \begin{pmatrix} r_1 & -a_1 & -b_1 & -c_1 \\ a_1 & r_1 & -c_1 & b_1 \\ b_1 & c_1 & r_1 & -a_1 \\ c_1 & -b_1 & a_1 & r_1 \end{pmatrix} \begin{pmatrix} r_2 \\ a_2 \\ b_2 \\ c_2 \end{pmatrix}. \quad (6)$$

To implement a quaternion convolutional (q-Conv) layer in numerical programming, we will regard the two quaternions as a 4×4 matrix and a 4×1 column matrix, respectively:

$$q_1 \doteq \begin{pmatrix} r_1 & -a_1 & -b_1 & -c_1 \\ a_1 & r_1 & -c_1 & b_1 \\ b_1 & c_1 & r_1 & -a_1 \\ c_1 & -b_1 & a_1 & r_1 \end{pmatrix} \quad \text{and} \quad q_2 \doteq \begin{pmatrix} r_2 \\ a_2 \\ b_2 \\ c_2 \end{pmatrix}. \quad (7)$$

More details of quaternion algebra are described in Appendix B.

A conventional CNN contains a real-valued convolutional layer to execute the convolution of the input and the kernel. Let the input F have the shape: $H_i \times W_i \times C_i$ (Height \times Width \times Channel) and the shape of the kernel K be $H_k \times W_k \times C_i \times C_f$. The convolution will produce an output O , $O = F * K$, whose elements are

$$O_{i',j',t'} = \sum_i^{H_k} \sum_j^{W_k} \sum_t^{C_i} F_{i'+i-1,j'+j-1,t} \cdot K_{i,j,t,t'}. \quad (8)$$

Here the stride is assumed to be 1 both in the width and the height directions. The indices i and j are spatial

indicators, t is the index of channel in the input feature map and t' is the kernel index. The shape of the output will be $(H_i - H_k) \times (W_i - W_k) \times C_f$.

Assume that the input has four components. To uncover the entanglement among components through CNN, we will utilize the quaternion product. Now, we introduce another dimension-Depth—which is four, as a quaternion number of four components. Both of the input F and the kernel K have Depth of four as two quaternion numbers. The product of F and K will have Depth of four as a quaternion in Eq. (5). Referring to Eq. (7) where we show a matrix representation to implement quaternion algebra and thinking of F as q_1 and K as q_2 in Eq. (7), we transform the Depth-four input F into a 4×4 matrix, $F^{(l,s)}$, and keep the kernel K still of Depth 4, $K^{(l)}$, where $l, s = 1, \dots, 4$. The product of F and K , say O , will have Depth of four as shown in Eq. (9). We remark that the products between components of F and K are convolution operations as Eq. (8).

$$O_{i',j',t'}^{(s)} = \sum_l^4 \sum_{i,j,t} F_{i'+i-1,j'+j-1,t}^{(s,l)} \cdot K_{i,j,t,t'}^{(l)}, \quad (9)$$

More specifically, we consider an input data as q_1 (four color squares on the left of Fig. 3) and four kernels encoded in q_2 , given in the following

$$\begin{cases} q_1 \doteq (r_1 \ a_1 \ b_1 \ c_1)^T \\ q_2 \doteq (r_2 \ a_2 \ b_2 \ c_2)^T \end{cases} =: K^{(\cdot)}. \quad (10)$$

The output feature maps $O \doteq (R \ A \ B \ C)^T$ is then calculated based on Eq. (5). As the first step, we permute

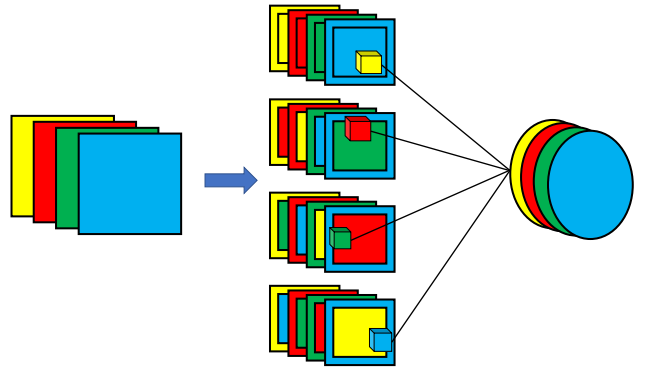


FIG. 3. Illustration of a quaternion convolutional layer. On the left, we start with the input q_1 having four quaternion components ((yellow, red, green, blue) stands for (r_1, a_1, b_1, c_1)). In the middle, q_1 is permuted to construct $\{F^{(l,s)}\}_{l=1}^4$ on which the convolution with four kernels $\{K^{(l)}\}_{l=1}^4$ is performed. A summation is taken for each Depth dimension to obtain the output feature map O on the right.

the order of q_1 to obtain

$$\begin{aligned} F^{(\cdot,1)} &= \begin{pmatrix} r_1 \\ a_1 \\ b_1 \\ c_1 \end{pmatrix}, F^{(\cdot,2)} = \begin{pmatrix} -a_1 \\ r_1 \\ c_1 \\ -b_1 \end{pmatrix}, \\ F^{(\cdot,3)} &= \begin{pmatrix} -b_1 \\ -c_1 \\ r_1 \\ a_1 \end{pmatrix}, F^{(\cdot,4)} = \begin{pmatrix} -c_1 \\ b_1 \\ -a_1 \\ r_1 \end{pmatrix} \end{aligned} \quad (11)$$

(see the four sets of squares in the middle of Fig. 3). We then convolute those four quaternions ($F^{(\cdot,l)}$ with $l = 1, 2, 3$ and 4) with four kernels ($K^{(l)}$ with $l = 1, 2, 3$ and 4) in the following way:

$$\begin{cases} F^{(\cdot,1)}K^{(1)} \doteq (r_1r_2 \ a_1r_2 \ b_1r_2 \ c_1r_2)^T \\ F^{(\cdot,2)}K^{(2)} \doteq (-a_1a_2 \ r_1a_2 \ c_1a_2 \ -b_1a_2)^T \\ F^{(\cdot,3)}K^{(3)} \doteq (-b_1b_2 \ -c_1b_2 \ r_1b_2 \ a_1b_2)^T \\ F^{(\cdot,4)}K^{(4)} \doteq (-c_1c_2 \ b_1c_2 \ -a_1c_2 \ r_1c_2)^T \end{cases}$$

, as shown in the middle of Fig. 3. Finally, we sum over the above four quaternions to get the output feature maps O , as shown on the right of Fig. 3.

$$O := \begin{pmatrix} R \\ A \\ B \\ C \end{pmatrix} = \begin{pmatrix} r_1r_2 - a_1a_2 - b_1b_2 - c_1c_2 \\ a_1r_2 + r_1a_2 - c_1b_2 + b_1c_2 \\ b_1r_2 + c_1a_2 + r_1b_2 - a_1c_2 \\ c_1r_2 - b_1a_2 + a_1b_2 + r_1c_2 \end{pmatrix}.$$

III. PRINCIPAL COMPONENT ANALYSIS

Principal component analysis (PCA) is a linear manifold learning that is to find the relevant basis set among data[55, 56].

We prepare eigenstates $|u_{\pm}\rangle$ of Eq. (1), where + (−) stands for the upper (lower) band. For a topological state, the phase cannot be well-defined over the whole BZ. Therefore, we can divide the whole BZ into two parts, in each part of them the topological wave function has continuously well-defined phase. We then choose two regions according to the sign of h_3 in Eq. (3):

$$\begin{aligned} |u_+\rangle &\doteq \frac{1}{\sqrt{2h_+(h_+ + h_3)}} \begin{pmatrix} h_+ + h_3 \\ h_1 + ih_2 \end{pmatrix}, \quad h_3 \geq 0, \\ |u_-\rangle &\doteq \frac{1}{\sqrt{2h_-(h_- + h_3)}} \begin{pmatrix} -h_1 + ih_2 \\ h_- + h_3 \end{pmatrix} \end{aligned} \quad (12)$$

and

$$\begin{aligned} |u_+\rangle &\doteq \frac{1}{\sqrt{2h_+(h_+ - h_3)}} \begin{pmatrix} h_1 - ih_2 \\ h_+ - h_3 \end{pmatrix}, \quad h_3 < 0, \\ |u_-\rangle &\doteq \frac{1}{\sqrt{2h_-(h_- - h_3)}} \begin{pmatrix} h_- - h_3 \\ -h_1 - ih_2 \end{pmatrix} \end{aligned} \quad (13)$$

where $h_{\pm} = \pm\sqrt{h_1^2 + h_2^2 + h_3^2}$. In this choice of gauge, the first (second) component of $|u_+\rangle$ ($|u_-\rangle$) is real-valued

when $h_3 \geq 0$, and the second (first) component of $|u_+\rangle$ ($|u_-\rangle$) is real-valued when $h_3 < 0$.

By translating $|u_{\pm}\rangle \doteq (\alpha_{\pm}, \beta_{\pm})^T$ with $\alpha_{\pm}, \beta_{\pm} \in \mathbb{C}$, into a quaternion number of four components, we have

$$q_{\pm} := \text{Re}(\alpha_{\pm}) + \text{Im}(\alpha_{\pm})\hat{\mathbf{i}} + \text{Re}(\beta_{\pm})\hat{\mathbf{j}} + \text{Im}(\beta_{\pm})\hat{\mathbf{k}}. \quad (14)$$

(a brief introduction of the quaternion number can be seen in Appendix B). To see the correlation of states over \vec{k} , we define the quantity F to be the quaternion-based convolutions:

$$\begin{aligned} F(\vec{p}) &:= q_{+}^* \circledast q_{+}[\vec{p}] - q_{-}^* \circledast q_{-}[\vec{p}] \quad \text{with} \\ q_{\pm}^* \circledast q_{\pm}[\vec{p}] &:= \sum_{\vec{k} \in \text{BZ}} q_{\pm}^*(\vec{k}) q_{\pm}(\vec{p} - \vec{k}), \end{aligned} \quad (15)$$

where q^* is the conjugate of q . It can be proved that F is real-valued. Therefore, $F(\vec{p})$ of all \vec{p} in the BZ based on a given Hamiltonian can be analysed by using PCA.

We collected various F of all $\vec{k} \in \text{BZ}$ within seven topological phases as the dataset for PCA. For each topological phases, 30 F 's were prepared, so the total amount of data was 210. The data for six non-trivial phases were generated based on Eq. (3) with $m = \pm 1$ (the sign of m determines the sign of C). For the trivial phase, we prepared five data points from each of six combinations of $\{c, m\}$, where $c \in \{1, 2, 3\}$ and $m \in \{3, -3\}$, and then there are totally 30 data. To augment the number of data, we add Gaussian noises $\delta\mathbf{h}$ at every \vec{k} of the model [Eq. (3)] such that $\mathbf{h} \rightarrow \mathbf{h} + \delta\mathbf{h}$ without closing the band gap.

In Fig. 4, we present various noiseless F generated from Eq. (3) with different c and m . It is notable that F

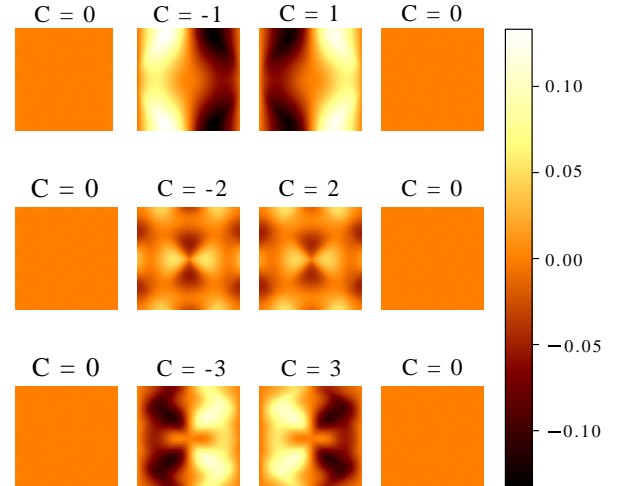


FIG. 4. The maps of the function F without noise in the BZ. Three rows are for $c = 1, 2$ and 3 in Eq. 3 from top to bottom; four columns from left to right are for $m = -3, -1, 1$ and 3. The corresponding Chern number C is tagged with each panel.

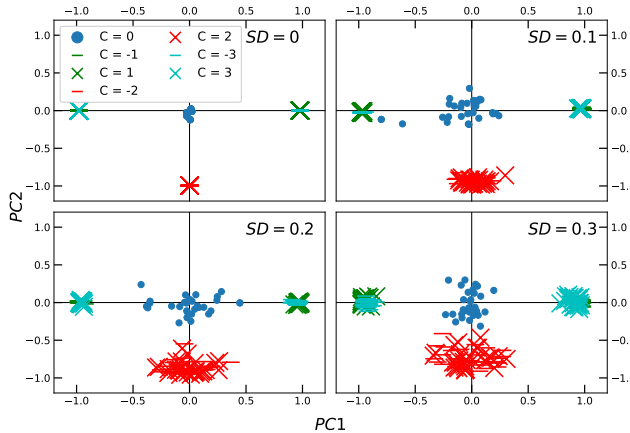


FIG. 5. PCA of seven topological phases with various noise. The symbols with corresponding Chern numbers are marked in the legend.

for $C = 0$ are featureless, F for $C = \pm 1$ have a dipole moment, and F for $C = \pm 2$ have a quadrupole moment, and F for $C = \pm 3$ seemingly have a primary dipole and a secondary quadrupole moment. The remarkable features imply that the convolution function F is a good choice for topological classifications.

We examine data with the standard deviation (SD) equal to 0, 0.1, 0.2 and 0.3 respectively, and show the first two PCs of 210 pieces of data for each SD in Fig. 5. In Fig. 5, it is evident that data are clustered into four groups and their variances increase with SD. PCA is successful to separate different topological phases into different clusters. However, some clusters contain two topological phases of Chern numbers: $\{+1, -3\}$, $\{-1, +3\}$, and $\{+2, -2\}$. The C modulo 4 resemblance has also been observed in a previous study [23]. We find that including more PCs helps separate different classes in each cluster.

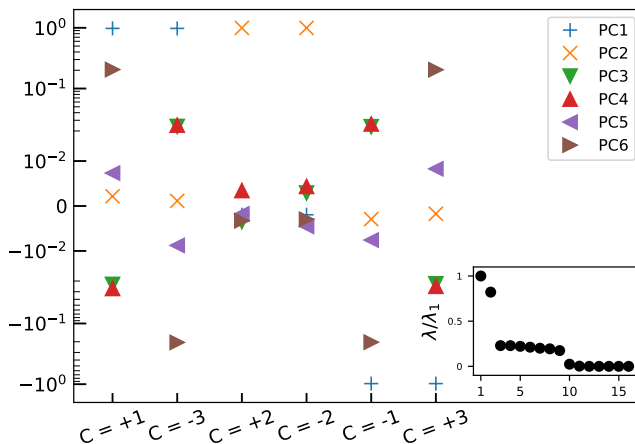


FIG. 6. Magnitude of projection (logarithmic scale) from non-trivial data onto first six principal components. Inset: The first 16 principal values of PCA. (normalized by maximal λ_1)

ter. Figure 6 shows first six PCs of data in topologically non-trivial phases, where PC_x denotes the x -th PC component. One can find that PC_1 and PC_2 in each pair of $\{+1, -3\}$, $\{-1, +3\}$, and $\{+2, -2\}$ are nearly identical, as also shown in Fig. 5. By including PC_3 – PC_6 into the analysis, all topological classes are completely classified. Via the proposed convolution, topological states can be successfully classified by using PCA, a linear machine for classification.

IV. SUPERVISED LEARNING OF CNN AND THE QCNN

A. Datasets

The input data are normalized spin configurations \mathbf{n} , laying on a 40×40 square lattice with periodic boundary conditions, and their corresponding topological phases are labels with one-hot encoding. We prepared four datasets: training, validation, testing and prediction dataset. The first three datasets are well known in conventional deep learning procedure [57]. To understand whether our machine can also classify unseen spin configuration, we prepare a prediction dataset that includes a few types of spin configurations never seen by the machine during the training process.

The data pool containing training and validation datasets is constructed as follows. Based on the Eq. (3), we firstly prepared 5760 data points of \mathbf{n} of nine topological phases with Chern number ranging from -4 to 4 so that each phase contain 640 data points. Additionally, we add 360 data points for spin vortex which belongs to the trivial phase. A spin-vortex has an in-plane spin texture that winds around a center, which is generated by setting one of three components in Eq. (3) to be zero. By including spin vortices, the machine learn the difference between 3D winding (non-trivial) and 2D winding (trivial) spin configurations (more details are described in the Appendix A). After the training process, the trained machine is scored by a testing dataset with the same composition of nine phases as that in the training (and validation) dataset. Importantly, without changing the topologies, the Gaussian distributed random transition and random rotation imposed on these three datasets can increase the diversity of dataset and enhance the ability of generalization of the trained machine.

The prediction dataset contains six categories of spin configurations. The first category is generated with m uniformly distributed from $+3$ to -3 . In the second and the third categories, we change the sign of n_z (the second category) and swapping n_y and n_z of \mathbf{n} (the third category). Finally, we consider three categories for trivial states, which are ferromagnetic (FM), conical ($\epsilon \neq 0$)

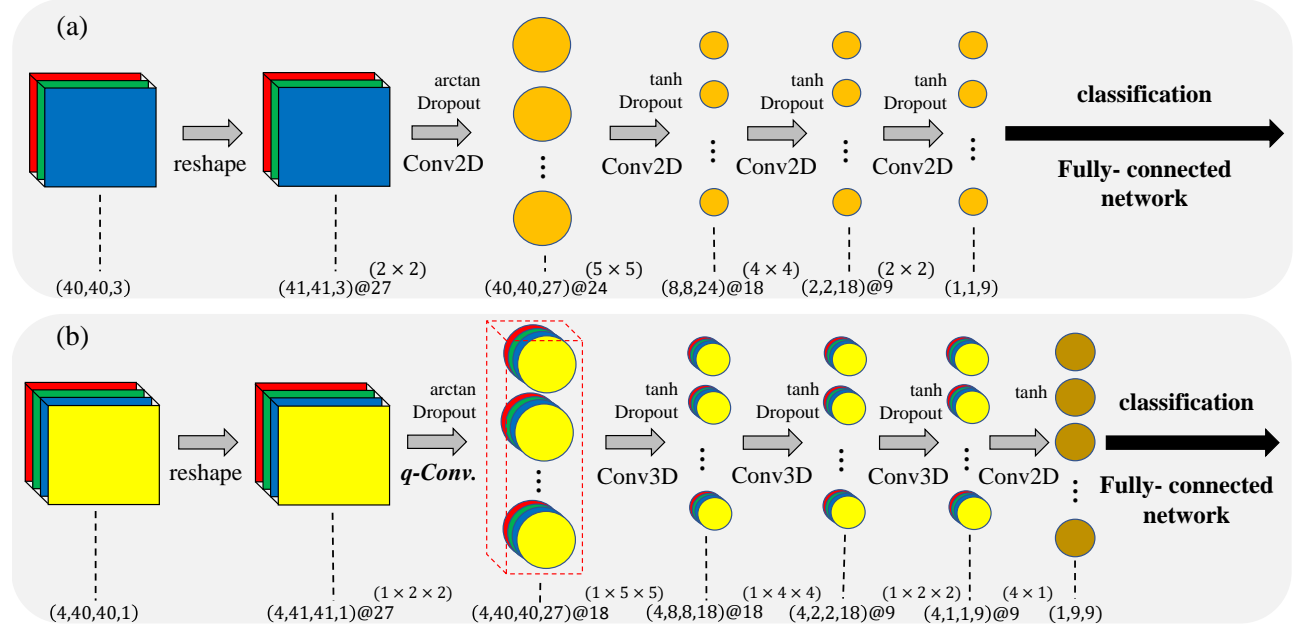


FIG. 7. Framework of (a) the CNN and (b) the qCNN classifier. The shape of data is $L_x \times L_y \times \text{(number of channels)}$. The number appended after the symbol “@” stands for the number of filters convolved with the data, and the number just above is the filter size. The number of tuneable network parameters of CNN (qCNN) is 24,252 (19,350).

and helical ($\epsilon = 0$) states, based on the following formula:

$$\mathbf{n}_{\text{spiral/conical}}(\vec{k}) = \begin{pmatrix} \sqrt{1 - \epsilon^2} \cos(k_x + k_y) \\ \sqrt{1 - \epsilon^2} \sin(k_x + k_y) \\ \epsilon \end{pmatrix}. \quad (16)$$

FM can be viewed as 1D uncompleted winding configuration while conical and helical can be viewed as 2D uncompleted ones. In total, we prepared six categories for the prediction dataset. More details about data preparations will be described in Appendix A.

For the conventional CNN, we use \mathbf{n} as the input data. For the qCNN, in order to feed the input data into the qCNN classifier, we transform the 3D spin vector into an unit pure quaternion,

$$(n_x, n_y, n_z) \in \mathbb{R}^3 \mapsto (0, n_x, n_y, n_z) \in \mathbb{H}, \quad (17)$$

where the scalar part (the first component) is zero and the vector part is \mathbf{n} .

B. network structure and performance

We implement a qCNN classifier with a quaternion convolution (q-Conv) layer as the first layer [see red dotted cube in Fig. 7(b)], and the operations in a q-Conv layer are based on the quaternion algebra. Then the next three layers are conventional 3D convolutional layers. Details of the quaternion algebra and the keynote of a qCNN are explained in Appendix B. For comparison, we also set up a conventional CNN classifier by replacing the q-Conv layer by a conventional 2D convolutional layer, and

appending three conventional 2D convolutional layers to the first layer. The architecture of these two classifiers are shown in Fig. 7. Note that the data in the qCNN has one more rank than that in CNN, and in numerical programs, this extra dimension—*Depth* is used to store the quaternion [referred to Eq. (17)]. As you can see in the Fig. 7, the architecture of the qCNN is one layer more than the CNN’s, the total network parameters of the qCNN is however less than the CNN’s. This is one advantage of the qCNN over the conventional CNN.

In order for classifiers to satisfy some physically reasonable conditions, three special designs are needed. Firstly, we extend the k points out of the BZ by padding the input data according to the periodic boundary conditions [58]. Secondly, a convolutional layer (q-Conv layer in the qCNN) with arctangent activation function is then adopted, which contains 27 filters of kernel size 2×2 . This layer executes an “overlapping” feature mapping. (Figure 8 illustrates how the “overlapping” and “non-overlapping” feature mapping can be manipulated by varying the size of stride.) Thirdly, we shrink the k space of data into “a point” by three non-overlapping convolutional layers. In the qCNN, three 3D convolutional layers are applied while keeping four Depths independent. In particular, we additionally append a 2D convolutional layer to make combination Depths-wisely. Specifically, this layer with 9 filters of kernel size 4×1 transforms data from 4×9 to 1×9 , where each of nine neurons corresponds to one topological class. In comparison, the conventional CNN shrinks the k -space to a point in each of nine *Channels*, where the dimension is integrated out after the convolution. More details and descriptions are

relative to the SEC. V.

In the following, we perform both the qCNN and conventional CNN trainings. The learning curves of both machines are shown in Fig. 9. The CNN machine (orange and light orange lines) jumps over a big learning barrier at around the 700th epoch. After that, the training and the validation accuracy (orange and light orange line respectively) are separated and do not converge up to end of this training process. Even though the same training (and validation) dataset is used in the training process, the learning curves of the qCNN machine (blue and light blue lines) are qualitatively different. The training and the validation accuracy are separated around 90th epoch, but the difference between these two accuracies decreases with increasing epochs. After the training procedure finished, the qCNN (CNN) machine gets 99.67% (94.12%) testing accuracy. This difference in accuracy results from the spin-vortex dataset, where the qCNN works well but CNN dose not.

The trained machines are ready to do prediction, and the result is shown in Fig. 10. In Fig. 10, since the first category contains \mathbf{n} of uniformly distributed m , where

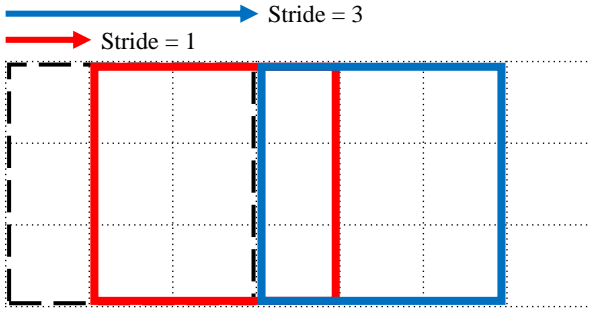


FIG. 8. Schematic of “overlap” convolution (red solid) and “non-overlap” convolution (blue solid) from a 3×3 filter (black dotted) over data. The blue solid square is a signal movement from the filter, and the size of stride is the same as the length of filter, thus each movement of this filter is “non-overlap”.

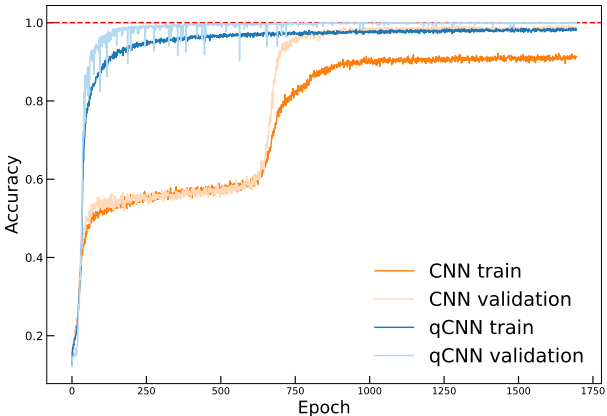


FIG. 9. Learning curves of the qCNN and CNN classifiers. By applied *Dropout*, the validation is greater than the training.

a few data points are very close to the phase boundaries $m \approx \{0, \pm 2\}$, the accurate rate of the the qCNN is slightly low at 96%. For the second and third categories, we choose $m = \pm 1$, away from the phase transition points, and the performance is nearly perfect. For the uncompleted winding configurations, the qCNN, different from the conventional CNN, can accurately classifies FM, helical and conical states after learning the spin-vortex states. This is the main advantage of the qCNN over the conventional CNN, which is expected to result from the quaternion algebra.

V. DISCUSSIONS

On PCA the reason why we choose spinor state vector $|u\rangle$, not the spin normalized vector \mathbf{n} as data is that the gauge discontinuities exist in the non-trivial $|u\rangle$, but not in \mathbf{n} ’s. It turns out that the function F can detect the existence of this discontinuity so that trivial and non-trivial states can be distinguished by PCA. Above statement is further supported by the relation between $|u\rangle$ and \mathbf{n} in pure state, which is known as

$$\mathbf{n}(\vec{k}) = \langle u_+(\vec{k}) | \boldsymbol{\sigma} | u_+(\vec{k}) \rangle. \quad (18)$$

In Eq. (18), the $U(1)$ ambiguity of $|u\rangle$ is eliminated effectively, thus, there is no discontinuities to be detected by PCA in \mathbf{n} . There is another issue if we use \mathbf{n} as the data in PCA. If we encode $\mathbf{n} = (n_x, n_y, n_z)$ into a quaternion in the following form,

$$q := (0, n_x, n_y, n_z),$$

the corresponding convolution [Eq. (15)] will not depend on the sign of m . It can be shown that there exists one

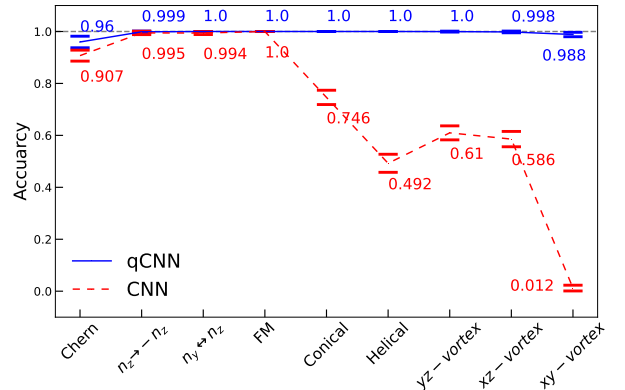


FIG. 10. The performance of the qCNN (blue line) and CNN (red dashed line) on the prediction datasets. Numbers tagged are the values of the accuracies. Standard deviations (by error bars) are also provided. The qCNN outperforms the conventional CNN on all prediction datasets, especially on three spin-vortex ones

point $\vec{k}' \rightarrow \vec{p}_0 - \vec{k} + \pi$ in BZ such that

$$n_z(\vec{k}, m_0)n_z(\vec{p}_0 - \vec{k}, m_0) = n_z(\vec{k}', -m_0)n_z(\vec{p}_0 - \vec{k}', -m_0).$$

That is, for two spin configurations with opposite sign m_0 , their n_z products are equal at \vec{k} and \vec{k}' respectively. As shown in Eq. (3), m shows up only in the n_z component. Therefore, after the integration over the whole BZ, the convolution is independent of the sign of m and there is no feature for PCA to discriminate distinct topological states.

On qCNN, there are several possible factors promoting the performance of our supervised learning machine. The first one is that the size of filter in the first convolutional layer is 2×2 with stride = 1, which means the machine can collect spin information among four nearest neighbors [see Fig. 11(b)]. We know that the Chern number is the integral of the Berry curvature in the BZ, and the Berry curvature is twice of the solid angle. A solid angle Ω subtended by three normalized vectors $\vec{a}, \vec{b}, \vec{c}$, can be calculated using the following equation:

$$\tan \frac{\Omega}{2} = \frac{|\vec{a} \cdot (\vec{b} \times \vec{c})|}{1 + \vec{a} \cdot \vec{b} + \vec{b} \cdot \vec{c} + \vec{c} \cdot \vec{a}}. \quad (19)$$

Our choice of the size of the filter in the first hidden layer is the minimal of 2×2 that mixes only the nearest-neighboring spins. In this way, it is very possible to enforce the machine to notice the solid angle extended in this plaquette. The second factor is the quaternion product. Recall that the conventional CNN might correlate spins \mathbf{n} 's in neighboring \vec{k} 's due to the feature map through the kernel. However, the map does not mix the components of spins. In comparison, the qCNN is more efficient for it directly entangle spins via the quaternion product. It is this entanglement of spin components by the quaternion product that makes the scalar and vector products in calculating the solid angle (see Eq. (19)) become possible to be realized by the machine. As a solid angle involves at least three spins and the feature map by the kernel is just linear, a nonlinear transformation is crucial to create high-order (three spins) terms in the expansion. Based on this argument, the third factor is the non-linear activation function [59], which is an arctangent function in this work. Based on Eq. (19), the

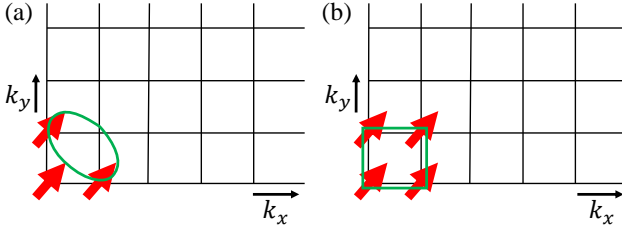


FIG. 11. (a) Three nearest neighborhood spin vectors will contribute a solid angle, and (b) four nearest neighbors are enclosed by the filters in the first convolutional layer.

calculation of a solid angle involves the arctan operation. Therefore, we expect that using the arctangent function as the activation function can further help the machine to learn correct representations. This idea is further supported by the results shown in Fig. 12, where the arctangent activation function outperforms the ReLU and tanh activation functions over nine different datasets. In summary, several factors are combined to enhance the performance of our machine as follows. The quaternion-based operations in the q-Conv layer mix not only different components of a spin $\mathbf{n}(\vec{k}_0)$ but also neighbouring spins, say $\mathbf{n}(\vec{k}_0)$ and $\mathbf{n}(\vec{k}_1)$. When these linear combinations are fed into the non-linear activation functions in our qCNN, the output can be viewed as an expansion of a non-linear function, which may contain a term having both the scalar- and vector-product of neighboring spins, similar to that in Eq. (19). Therefore, in the optimization process, combined with the effect of choosing the size of filter to be 2×2 , the machine may keep increasing the weight of a solid-angle-related term and eventually learn to classify the topological phases based on the calculated solid angles.

Also, adding some noises to the training dataset helped our supervised-learning machine to learn the generic feature of our data. We found that when the training data was generated directly from Eq. (3) without adding any noise, the machine worked well for training and testing datasets but had poor performance on all the prediction dataset. This could be understood by noting that topology is determined by the sign of m , which appears only in the z component in Eq. (3). By using the dataset without noises, the machine may learn to classify states only by looking at the z -component but not extracting the full information from the full configuration. When we gave random transition and rotation to each training data, the machine had to examine all three components in order to have correct predictions. From our observations, the performance on the prediction dataset was remarkably enhanced when the noise was added, which supports our ideas.

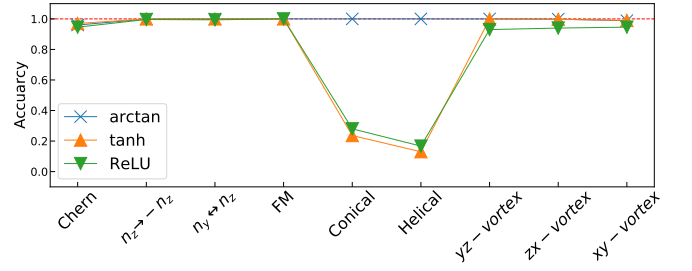


FIG. 12. Comparison between three activation function applied in the first layer of the qCNN classifier.

VI. CONCLUSIONS

In summary, we classify topological phases with distinct Chern numbers via two types of machine-learning algorithms. For the unsupervised part, we propose a quaternion-based convolution to transform the topological states into the input data. With this convolution, distinct topological states are successfully classified by PCA, a linear machine for classification.

We then go to the supervised learning part where, in contrast to the conventional CNN, we successfully use the qCNN to classify different topological phases. This work demonstrates the power of quaternion-based algorithm, especially for the topological systems with the Chern number as the topological invariants.

ACKNOWLEDGMENTS

This study is supported by the Ministry of Science and Technology (MoST) in Taiwan under grant No. 108-2112-M-110-013-MY3. M.R.L. and W.J.L. contributed equally to this work.

Appendix A: Data preparation

Training dataset— The normalized spin configurations $\mathbf{n}(\vec{k})$ are given in the following [referred to the Eq. (3)]

$$\mathbf{n} := \mathbf{h}/|\mathbf{h}|, \quad \text{where}$$

$$\mathbf{h}(\vec{k})[m, c] = \begin{pmatrix} \text{Re}[(\sin k_x - i \sin k_y)^c] \\ -\text{Im}[(\sin k_x - i \sin k_y)^c] \\ \cos k_x + \cos k_y + m \end{pmatrix}$$

in a 40×40 square lattice with periodic boundary conditions. For each $c \in \{1, 2, 3, 4\}$, we generated 1440 spin configurations. That is totally 5760 normalized spin configurations $\mathbf{n}(\vec{k})$ throughout nine topological states of Chern number ranging from -4 to 4. For given c and m , each of spin configurations is under data augmentation and Gaussian noise. The details are in the following. For a given spin configuration, $\mathbf{n}(\vec{k})$, we produce its multiple derivatives through a random translation (\mathcal{T}) and a random rotation (\mathcal{R}) in three dimensions:

$$\mathbf{n}(\vec{k}) \xrightarrow{\mathcal{T}} \mathbf{n}(\vec{k} + \vec{p}_0) \xrightarrow{\mathcal{R}} \mathbf{n}'(\vec{k} + \vec{p}_0) \xrightarrow{\mathcal{G}} \mathbf{n}'(\vec{k} + \vec{p}_0) + \Delta \mathbf{n}'(\vec{k}) \quad (\text{A1})$$

where \vec{p}_0 is a random displacement in k space, and the operation \mathcal{R} stands for applying the 3×3 rotation matrix on whole configuration with arbitrary Euler angles. After data augmentation, we further applied three-component Gaussian noise (\mathcal{G}) with 0.1π standard deviation (SD) at randomly chosen 30 out of 1600 spin vectors for each spin configuration.

Here, we provide more details about the data generation. For each c we generated four sets $S_1^{(c)}$, $S_2^{(c)}$, $S_3^{(c)}$ and

$S_4^{(c)}$. Each of the first-two sets contains 640 topologically nontrivial states:

$$\begin{aligned} S_1^{(c)} &= \{\mathbf{n} \mid m \in [-1.9, -0.1]\}, \\ S_2^{(c)} &= \{\mathbf{n} \mid m \in [0.1, 1.9]\}. \end{aligned}$$

Each of the rest two sets contains 80 topologically trivial states:

$$\begin{aligned} S_3^{(c)} &= \{\mathbf{n} \mid m = -3\}, \\ S_4^{(c)} &= \{\mathbf{n} \mid m = 3\}. \end{aligned}$$

That is, for each c we have 1280 nontrivial spin configurations and 160 trivial ones. Thus, the 5760 spin configurations are evenly divided into nine topological phases, each of which contains 640 spin configurations. In the training data, we also include 360 spin vortice states, which are $C = 0$ states, according to the following models:

$$\mathbf{h}_{yz}(\vec{k}) = \begin{pmatrix} 0 \\ -\text{Im}[(\sin k_x - i \sin k_y)^c] \\ \cos k_x + \cos k_y + m \end{pmatrix} \quad (\text{A2})$$

$$\mathbf{h}_{xz}(\vec{k}) = \begin{pmatrix} \text{Re}[(\sin k_x - i \sin k_y)^c] \\ 0 \\ \cos k_x + \cos k_y + m \end{pmatrix} \quad (\text{A3})$$

$$\mathbf{h}_{xy}(\vec{k}) = \begin{pmatrix} \text{Re}[(\sin k_x - i \sin k_y)^c] \\ -\text{Im}[(\sin k_x - i \sin k_y)^c] \\ 0 \end{pmatrix} \quad (\text{A4})$$

For each c , 30 spin configurations are generated using each of the models above with uniformly distributed m ranging from -3 to 3. We therefore have totally 360 trivial states generated using different c and m . After the process, we have totally 6120 spin configurations as the training dataset.

After generating the training dataset, 25% of the training data are assigned as the validation dataset (light color lines in Fig. 9). Therefore, two dataset are prepared under data augmentation and noise for the supervised learning procedure.

Testing dataset— In addition to the training and validation dataset, we prepare extra 1224 spin configurations as the testing dataset, with the same composition as the training and validation datasets. This dataset is prepared for scoring the trained classifiers.

Prediction dataset— The prediction dataset is an extra dataset, different from the aforementioned three datasets. It consists of six categories, each of which is not seen by the machine during the training process. This dataset is processed by the data augmentation but without adding the Gaussian noise. The six categories are constructed as following. The First category, the

“chern” category, is a set S which is generated from Eq. (3) with 30 m ’s uniformly ranging from -3 to 3 for c :

$$S = \{\mathbf{n}^{(c)} \mid c = 1, 2, 3, 4, m = -3 + \frac{6i}{29}, i = 0, \dots, 29\}$$

As a reminder, this category is different from the training dataset. The training data includes the specific $m = \pm 3$ at trivial phase, and two intervals $\{[-1.9, -0.1]\}$ and $[0.1, 1.9]\}$ at nontrivial phases. Therefore, 20% of this category is close to the phase transition $m \approx \{0, +2, -2\}$.

The next two categories are generated based on the Eq. (3) with $m = \pm 1$. The first one is constructed by changing the sign of the z -component:

$$\begin{aligned} \mathbf{h}(\vec{k}) &= \begin{pmatrix} \operatorname{Re}[(\sin k_x - i \sin k_y)^c] \\ -\operatorname{Im}[(\sin k_x - i \sin k_y)^c] \\ \cos k_x + \cos k_y + m \end{pmatrix} \\ &\rightarrow \begin{pmatrix} \operatorname{Re}[(\sin k_x - i \sin k_y)^c] \\ -\operatorname{Im}[(\sin k_x - i \sin k_y)^c] \\ -\cos k_x - \cos k_y - m \end{pmatrix} = \mathbf{h}'(\vec{k}). \end{aligned}$$

The second one is constructed by swapping the y -component and the z -component:

$$\begin{aligned} \mathbf{h}(\vec{k}) &= \begin{pmatrix} \operatorname{Re}[(\sin k_x - i \sin k_y)^c] \\ -\operatorname{Im}[(\sin k_x - i \sin k_y)^c] \\ \cos k_x + \cos k_y + m \end{pmatrix} \\ &\rightarrow \begin{pmatrix} \operatorname{Re}[(\sin k_x - i \sin k_y)^c] \\ \cos k_x + \cos k_y + m \\ -\operatorname{Im}[(\sin k_x - i \sin k_y)^c] \end{pmatrix} = \mathbf{h}'(\vec{k}). \end{aligned}$$

The next two categories, called conical and helical spin configurations, are generated based on the following equation

$$\mathbf{n}_{\text{spiral/conical}}(\vec{k}) = \begin{pmatrix} \sqrt{1 - \epsilon^2} \cos(k_x + k_y) \\ \sqrt{1 - \epsilon^2} \sin(k_x + k_y) \\ \epsilon \end{pmatrix}.$$

Here $\epsilon = 0$ is for the helical state and $0 < |\epsilon| < 1$ is for a conical state. The last category contains the ferromagnetic spin configurations where the z -component is a constant and x - and y -component are zero.

Appendix B: Quaternion

The quaternion number system were introduced by Irish mathematician William Rowan Hamilton in 1843 as an extension of the complex numbers. A quaternion number q is composed of four real numbers r, a, b and c to be

$$q = r + a\hat{\mathbf{i}} + b\hat{\mathbf{j}} + c\hat{\mathbf{k}}, \quad (\text{B1})$$

where $\{\mathbf{1}, \hat{\mathbf{i}}, \hat{\mathbf{j}}, \hat{\mathbf{k}}\}$ is the basis. Sometimes it is written as $q = (r, \vec{v})$ or $q = (r, a, b, c)$ in short. Here r is called the scalar (or real) part of the quaternion and $\vec{v} = (a, b, c)$ the

vector (or imaginary) part. A quaternion without scalar part $q = (0, a, b, c)$ is called *pure quaternion*. Similar to the imaginary number,

$$\hat{\mathbf{i}}^2 = \hat{\mathbf{j}}^2 = \hat{\mathbf{k}}^2 = \hat{\mathbf{i}}\hat{\mathbf{j}}\hat{\mathbf{k}} = -\mathbf{1}. \quad (\text{B2})$$

Importantly, the algebra of quaternions is noncommutative, based on

$$\begin{aligned} \mathbf{1}\hat{\mathbf{i}} &= \hat{\mathbf{i}}\mathbf{1} = \hat{\mathbf{i}}, \quad \mathbf{1}\hat{\mathbf{j}} = \hat{\mathbf{j}}\mathbf{1} = \hat{\mathbf{j}}, \quad \mathbf{1}\hat{\mathbf{k}} = \hat{\mathbf{k}}\mathbf{1} = \hat{\mathbf{k}}, \\ \hat{\mathbf{i}}\hat{\mathbf{j}} &= -\hat{\mathbf{j}}\hat{\mathbf{i}} = \hat{\mathbf{k}}, \quad \hat{\mathbf{j}}\hat{\mathbf{k}} = -\hat{\mathbf{k}}\hat{\mathbf{j}} = \hat{\mathbf{i}}, \quad \text{and} \quad \hat{\mathbf{k}}\hat{\mathbf{i}} = -\hat{\mathbf{i}}\hat{\mathbf{k}} = \hat{\mathbf{j}}. \end{aligned} \quad (\text{B3})$$

The conjugate of the quaternion is defined to be

$$q^* = r - a\hat{\mathbf{i}} - b\hat{\mathbf{j}} - c\hat{\mathbf{k}}, \quad (\text{B4})$$

and the norm is given by

$$\|q\| = \sqrt{qq^*} = \sqrt{r^2 + a^2 + b^2 + c^2}. \quad (\text{B5})$$

Therefore the inverse of q is defined as

$$q^{-1} := \frac{q^*}{\|q\|^2}. \quad (\text{B6})$$

If q is unit quaternion, then their inverse is exactly their conjugate. The multiplication (so-called Hamilton product) of two quaternions $q_1 = (r_1, a_1, b_1, c_1)$ and $q_2 = (r_2, a_2, b_2, c_2)$ is given by

$$\begin{aligned} q_1 q_2 &= (r_1 r_2 - a_1 a_2 - b_1 b_2 - c_1 c_2) \\ &\quad + (a_1 r_2 + r_1 a_2 - c_1 b_2 + b_1 c_2)\hat{\mathbf{i}} \\ &\quad + (b_1 r_2 + c_1 a_2 + r_1 b_2 - a_1 c_2)\hat{\mathbf{j}} \\ &\quad + (c_1 r_2 - b_1 a_2 + a_1 b_2 + r_1 c_2)\hat{\mathbf{k}} \\ &= (r_1 r_2 - \vec{v}_1 \cdot \vec{v}_2, r_1 \vec{v}_2 + r_2 \vec{v}_1 + \vec{v}_1 \times \vec{v}_2). \end{aligned} \quad (\text{B7})$$

To realize the algebra in Eqs. (B2) and (B3), one can choose the $\mathcal{M}(4, \mathbb{R})$ representation for the quaternion numbers with

$$\begin{aligned} \mathbf{1} &\doteq \begin{pmatrix} 1 & 0 & 0 & 0 \\ 0 & 1 & 0 & 0 \\ 0 & 0 & 1 & 0 \\ 0 & 0 & 0 & 1 \end{pmatrix}, \quad \hat{\mathbf{i}} \doteq \begin{pmatrix} 0 & -1 & 0 & 0 \\ 1 & 0 & 0 & 0 \\ 0 & 0 & 0 & -1 \\ 0 & 0 & 1 & 0 \end{pmatrix}, \\ \hat{\mathbf{j}} &\doteq \begin{pmatrix} 0 & 0 & -1 & 0 \\ 0 & 0 & 0 & 1 \\ 1 & 0 & 0 & 0 \\ 0 & -1 & 0 & 0 \end{pmatrix}, \quad \text{and} \quad \hat{\mathbf{k}} \doteq \begin{pmatrix} 0 & 0 & 0 & -1 \\ 0 & 0 & -1 & 0 \\ 0 & 1 & 0 & 0 \\ 1 & 0 & 0 & 0 \end{pmatrix}, \end{aligned}$$

so that

$$q \doteq \begin{pmatrix} r & -a & -b & -c \\ a & r & -c & b \\ b & c & r & -a \\ c & -b & a & r \end{pmatrix}.$$

Reversely,

$$r = \frac{1}{4}\operatorname{tr}(q), \quad a = -\frac{1}{4}\operatorname{tr}(\hat{\mathbf{i}}q), \quad b = -\frac{1}{4}\operatorname{tr}(\hat{\mathbf{j}}q), \quad c = -\frac{1}{4}\operatorname{tr}(\hat{\mathbf{k}}q).$$

It is evident that in terms of matrices the commutativity of multiplication of quaternions dose not hold. Furthermore, in the matrix representation $q^* = q^T$, conjugation of a quaternion being equal to its transposition.

More specifically, an unit quaternion have a property $q^{-1} = q^* = q^T$ in the $\mathcal{M}(4, \mathbb{R})$ representations.

[1] J. Carrasquilla and R. G. Melko, Machine learning phases of matter, *Nature Physics* **13**, 431 (2017).

[2] E. Bedolla, L. C. Padierna, and R. Castañeda-Priego, Machine learning for condensed matter physics, *Journal of Physics: Condensed Matter* **33**, 053001 (2020).

[3] P. Mehta, M. Bukov, C.-H. Wang, A. G. Day, C. Richardson, C. K. Fisher, and D. J. Schwab, A high-bias, low-variance introduction to machine learning for physicists, *Physics reports* **810**, 1 (2019).

[4] M. J. Beach, A. Golubeva, and R. G. Melko, Machine learning vortices at the kosterlitz-thouless transition, *Physical Review B* **97**, 045207 (2018).

[5] N. Yoshioka, Y. Akagi, and H. Katsura, Learning disordered topological phases by statistical recovery of symmetry, *Physical Review B* **97**, 205110 (2018).

[6] D. Carvalho, N. A. García-Martínez, J. L. Lado, and J. Fernández-Rossier, Real-space mapping of topological invariants using artificial neural networks, *Physical Review B* **97**, 115453 (2018).

[7] O. Balabanov and M. Granath, Unsupervised learning using topological data augmentation, *Physical Review Research* **2**, 013354 (2020).

[8] O. Balabanov and M. Granath, Unsupervised interpretable learning of topological indices invariant under permutations of atomic bands, *Machine Learning: Science and Technology* **2**, 025008 (2020).

[9] E. Greplova, A. Valenti, G. Boschung, F. Schäfer, N. Lörch, and S. D. Huber, Unsupervised identification of topological phase transitions using predictive models, *New Journal of Physics* **22**, 045003 (2020).

[10] C.-T. Ho and D.-W. Wang, Robust identification of topological phase transition by self-supervised machine learning approach, *New Journal of Physics* **23**, 083021 (2021).

[11] L.-F. Zhang, L.-Z. Tang, Z.-H. Huang, G.-Q. Zhang, W. Huang, and D.-W. Zhang, Machine learning topological invariants of non-hermitian systems, *Physical Review A* **103**, 012419 (2021).

[12] B. Narayan and A. Narayan, Machine learning non-hermitian topological phases, *Physical Review B* **103**, 035413 (2021).

[13] L.-W. Yu and D.-L. Deng, Unsupervised learning of non-hermitian topological phases, *Physical Review Letters* **126**, 240402 (2021).

[14] Y. Zhang and E.-A. Kim, Quantum loop topography for machine learning, *Physical review letters* **118**, 216401 (2017).

[15] Q.-Q. Cheng, W.-W. Luo, A.-L. He, and Y.-F. Wang, Topological quantum phase transitions of chern insulators in disk geometry, *Journal of Physics: Condensed Matter* **30**, 355502 (2018).

[16] N. Sun, J. Yi, P. Zhang, H. Shen, and H. Zhai, Deep learning topological invariants of band insulators, *Physical Review B* **98**, 085402 (2018).

[17] Y. Zhang, P. Ginsparg, and E.-A. Kim, Interpreting machine learning of topological quantum phase transitions, *Physical Review Research* **2**, 023283 (2020).

[18] A. Kerr, G. Jose, C. Riggert, and K. Mullen, Automatic learning of topological phase boundaries, *Physical Review E* **103**, 023310 (2021).

[19] N. Kämäring, A. Dawid, K. Kottmann, M. Lewenstein, K. Sengstock, A. Dauphin, and C. Weitenberg, Unsupervised machine learning of topological phase transitions from experimental data, *Machine Learning: Science and Technology* **2**, 035037 (2021).

[20] B. S. Rem, N. Kämäring, M. Tarnowski, L. Asteria, N. Fläschner, C. Becker, K. Sengstock, and C. Weitenberg, Identifying quantum phase transitions using artificial neural networks on experimental data, *Nature Physics* **15**, 917 (2019).

[21] Y. Che, C. Gneiting, T. Liu, and F. Nori, Topological quantum phase transitions retrieved through unsupervised machine learning, *Physical Review B* **102**, 134213 (2020).

[22] M.-C. Chung, T.-P. Cheng, G.-Y. Huang, and Y.-H. Tsai, Deep learning of topological phase transitions from the point of view of entanglement for two-dimensional chiral p-wave superconductors, *Physical Review B* **104**, 024506 (2021).

[23] Y. Ming, C.-T. Lin, S. D. Bartlett, and W.-W. Zhang, Quantum topology identification with deep neural networks and quantum walks, *npj Computational Materials* **5**, 1 (2019).

[24] P. Zhang, H. Shen, and H. Zhai, Machine learning topological invariants with neural networks, *Physical review letters* **120**, 066401 (2018).

[25] N. Holanda and M. Griffith, Machine learning topological phases in real space, *Physical Review B* **102**, 054107 (2020).

[26] Y.-H. Tsai, K.-F. Chiu, Y.-C. Lai, K.-J. Su, T.-P. Yang, T.-P. Cheng, G.-Y. Huang, and M.-C. Chung, Deep learning of topological phase transitions from entanglement aspects: An unsupervised way, *Physical Review B* **104**, 165108 (2021).

[27] Y. Zhang, R. G. Melko, and E.-A. Kim, Machine learning z 2 quantum spin liquids with quasiparticle statistics, *Physical Review B* **96**, 245119 (2017).

[28] T. Mano and T. Ohtsuki, Application of convolutional neural network to quantum percolation in topological insulators, *Journal of the Physical Society of Japan* **88**, 123704 (2019).

[29] Z. Su, Y. Kang, B. Zhang, Z. Zhang, and H. Jiang, Disorder induced phase transition in magnetic higher-order topological insulator: A machine learning study, *Chinese Physics B* **28**, 117301 (2019).

[30] W. Lian, S.-T. Wang, S. Lu, Y. Huang, F. Wang, X. Yuan, W. Zhang, X. Ouyang, X. Wang, X. Huang, *et al.*, Machine learning topological phases with a solid-state quantum simulator, *Physical review letters* **122**, 210503 (2019).

[31] M. Richter-Laskowska, H. Khan, N. Trivedi, and M. M. Maśka, A machine learning approach to the berezinskii-kosterlitz-thouless transition in classical and quantum

models, arXiv preprint arXiv:1809.09927 (2018).

[32] W. Zhang, J. Liu, and T.-C. Wei, Machine learning of phase transitions in the percolation and x y models, *Physical Review E* **99**, 032142 (2019).

[33] J. F. Rodriguez-Nieva and M. S. Scheurer, Identifying topological order through unsupervised machine learning, *Nature Physics* **15**, 790 (2019).

[34] Y.-H. Tsai, M.-Z. Yu, Y.-H. Hsu, and M.-C. Chung, Deep learning of topological phase transitions from entanglement aspects, *Physical Review B* **102**, 054512 (2020).

[35] M. S. Scheurer and R.-J. Slager, Unsupervised machine learning and band topology, *Physical review letters* **124**, 226401 (2020).

[36] M. D. Caio, M. Caccin, P. Baireuther, T. Hyart, and M. Fruchart, Machine learning assisted measurement of local topological invariants, arXiv preprint arXiv:1901.03346 (2019).

[37] M. Trabelsi, P. Kakosimos, and H. Komurcugil, Mitigation of grid voltage disturbances using quasi-z-source based dynamic voltage restorer, in *2018 IEEE 12th International Conference on Compatibility, Power Electronics and Power Engineering (CPE-POWERENG 2018)* (IEEE, 2018) pp. 1–6.

[38] C. J. Gaudet and A. S. Maida, Deep quaternion networks, in *2018 International Joint Conference on Neural Networks (IJCNN)* (IEEE, 2018) pp. 1–8.

[39] D. García-Retuerta, R. Casado-Vara, A. Martin-del Rey, F. De la Prieta, J. Prieto, and J. M. Corchado, Quaternion neural networks: state-of-the-art and research challenges, in *International Conference on Intelligent Data Engineering and Automated Learning* (Springer, 2020) pp. 456–467.

[40] T. Isokawa, N. Matsui, and H. Nishimura, Quaternionic neural networks: Fundamental properties and applications, in *Complex-valued neural networks: utilizing high-dimensional parameters* (IGI global, 2009) pp. 411–439.

[41] T. Parcollet, M. Mørchid, and G. Linarès, A survey of quaternion neural networks, *Artificial Intelligence Review* **53**, 2957 (2020).

[42] N. Matsui, T. Isokawa, H. Kusamichi, F. Peper, and H. Nishimura, Quaternion neural network with geometrical operators, *Journal of Intelligent & Fuzzy Systems* **15**, 149 (2004).

[43] X. Zhu, Y. Xu, H. Xu, and C. Chen, Quaternion convolutional neural networks, in *Proceedings of the European Conference on Computer Vision (ECCV)* (2018) pp. 631–647.

[44] S. Hongo, T. Isokawa, N. Matsui, H. Nishimura, and N. Kamiura, Constructing convolutional neural networks based on quaternion, in *2020 International Joint Conference on Neural Networks (IJCNN)* (IEEE, 2020) pp. 1–6.

[45] T. Parcollet, Y. Zhang, M. Mørchid, C. Trabelsi, G. Linarès, R. De Mori, and Y. Bengio, Quaternion convolutional neural networks for end-to-end automatic speech recognition, arXiv preprint arXiv:1806.07789 (2018).

[46] E. Grassucci, E. Cicero, and D. Comminiello, Quaternion generative adversarial networks, in *Generative Adversarial Learning: Architectures and Applications* (Springer, 2022) pp. 57–86.

[47] E. Grassucci, D. Comminiello, and A. Uncini, A quaternion-valued variational autoencoder, in *ICASSP 2021-2021 IEEE International Conference on Acoustics, Speech and Signal Processing (ICASSP)* (IEEE, 2021) pp. 3310–3314.

[48] T. D. Nguyen, D. Phung, et al., Quaternion graph neural networks, in *Asian Conference on Machine Learning* (PMLR, 2021) pp. 236–251.

[49] B. Özcan, F. Kinli, and F. Kiraç, Quaternion capsule networks, in *2020 25th International Conference on Pattern Recognition (ICPR)* (IEEE, 2021) pp. 6858–6865.

[50] T. Parcollet, M. Ravanelli, M. Mørchid, G. Linarès, and R. De Mori, Speech recognition with quaternion neural networks, arXiv preprint arXiv:1811.09678 (2018).

[51] P. R. Girard, The quaternion group and modern physics, *European Journal of Physics* **5**, 25 (1984).

[52] P. R. Girard and W. E. Baylis, Quaternions, clifford algebras and relativistic physics, *SIAM review* **50**, 382 (2008).

[53] P. R. Girard, P. Clarysse, R. Pujol, R. Goutte, and P. Delachartre, Hyperquaternions: a new tool for physics, *Advances in Applied Clifford Algebras* **28**, 1 (2018).

[54] X.-L. Qi, Y.-S. Wu, and S.-C. Zhang, Topological quantization of the spin hall effect in two-dimensional paramagnetic semiconductors, *Phys. Rev. B* **74**, 085308 (2006).

[55] I. T. Jolliffe and J. Cadima, Principal component analysis: a review and recent developments, *Philosophical Transactions of the Royal Society A: Mathematical, Physical and Engineering Sciences* **374**, 20150202 (2016).

[56] Y. Ma and Y. Fu, *Manifold learning theory and applications*, Vol. 434 (CRC press Boca Raton, FL, 2012).

[57] F. Chollet, *Deep learning with Python* (Simon and Schuster, 2021).

[58] S. Efthymiou, M. J. S. Beach, and R. G. Melko, Super-resolving the ising model with convolutional neural networks, *Phys. Rev. B* **99**, 075113 (2019).

[59] H. R. Lin, M. Tegmark, and D. Rolnick, Why does deep and cheap learning work so well?, *Journal of Statistical Physics* **168**, 1223 (2017).